RSC Advances

PAPER

View Article Online
View Journal | View Issue

Cite this: *RSC Adv.*, 2025, **15**, 32929

Boron-/nitrogen-doped $Ti_3C_2T_x$ MXene quantum dot-based sensor for determining an acute kidney injury biomarker

Rijo Rajeev,[ab] Ann Mariella Babu[ab] and Anitha Varghese *[ab]

In this study, boron/nitrogen-doped $Ti_3C_2T_x$ MXene quantum dots (BNMQDs) were synthesized *via* a hydrothermal technique and successfully brush-coated on a carbon fiber paper (CFP)-based electrode to detect creatinine (crt). The prepared MQDs were characterized by employing transmission electron microscopy (TEM), Raman spectroscopy, X-ray photoelectron spectroscopy (XPS), infrared spectroscopy (IR), and X-ray diffraction (XRD) analysis to study their physicochemical properties. The electrochemical performance of the modified CFP-based sensors toward crt detection was analyzed by employing cyclic voltammetry (CV) and differential pulse voltammetry (DPV). $Ti_3C_2T_x$ MQDs were prepared using the hydrothermal method and further doped with B and N using boric acid and *p*-phenylene diamine, respectively. The morphology of the obtained BNMQDs was quasi-spherical and exhibited uniform size with scattered particle sizes ranging from 5 to 9.5 nanometers. Owing to several surface-active sites, edge effects, and quantum confinement, the synthesized MQDs demonstrated enhanced electrooxidation of crt. Compared to BMQDs and NMQDs, BNMQDs showed superior sensing performance, with a wide linear range of 0.104–135 μM and an LOD of 34.53 nM. The fabricated electrode also demonstrated high stability, reproducibility, and selectivity for the electrocatalytic oxidation of crt in real samples.

Received 23rd June 2025
Accepted 23rd August 2025

DOI: 10.1039/d5ra04474j

rsc.li/rsc-advances

1. Introduction

Crt is a critical biomarker formed as the product of crt metabolism and is present in muscle tissues and biological fluids, including blood and urine.[1,2] The average crt level in a healthy human body is 0.6–1.2 mg dL^{-1} in blood.[3,4] An increase or decrease in the crt level can lead to hyperthyroidism and hypothyroidism, respectively.[5,6] Such changes may also result in various other disorders, including weight loss, anemia, diabetes mellitus, and chronic kidney disease.[7,8] The analysis of crt levels is helpful for the diagnosis of thyroid disorders, renal dysfunction, and acute myocardial infarction.[9] Crt concentration is taken into consideration for analyzing the normal renal functioning compared to testing based on urea concentration, as protein intake does not affect its concentration in body fluids. The urine crt level indirectly indicates the concentration of crt and crt phosphate in the body and muscle tissues as they are directly proportional. Several techniques, including the Jaffe reaction method,[10] chromatography,[11] surface-enhanced Raman spectroscopy,[12] and chemiluminescence spectroscopy, have been reported for the detection of crt.[13] However, their utilization is limited due to the utilization of non-environmentally benign chemicals, tedious sample preparation procedures, involvement of high-end instruments, and the requirement of human labor. Therefore, electrochemical methods are promising as they are more rapid, selective, and sensitive.

Fekry *et al.* designed a sensor for crt detection by employing CPE with AgNPs/MWCNT/folic acid (FA). The synergistic contribution from both the MWCNTs and AgNPs led to an increased surface area, thereby inducing higher absorptivity of FA toward crt *via* the lone pair of e^-. These electron pairs on crt granted easy binding on the electrode *via* adsorption with FA and coordination with AgNPs. The developed sensor exhibited good stability, selectivity, a wide detection range (1×10^{-8} A–2×10^{-4} M), and an LOD of 0.008 mM.[14] Pandey and co-workers reported a selective and sensitive polymer–metal–carbon nanofiber nanocomposite-based electrochemical sensor for crt. PMB nanofibers produced ultra-enhancement of the surface area, improving the electrocatalytic ability towards crt. The fabricated sensor could exhibit a comprehensive linear response (0.5–900 ng ml^{-1}) and an LOD of 0.2 ng ml^{-1}.[15]

Recently, the focus has taken a massive shift towards utilizing nanosized or 0, 1, 2D materials compared to bulk materials.[16,17] The adoption of miniaturization improves their electronic properties, giving rise to interesting structural characteristics and leading to high applicability in varied fields.[18]

[a]*Department of Chemistry, Christ University, Bangalore, Karnataka, 560029, India. E-mail: anitha.varghese@christuniversity.in*

[b]*Centre for Renewable Energy and Environmental Sustainability, Christ University, Karnataka, 560 029, India*

Since its discovery in 2011, MXene has generated interest among researchers. MXene is classified among the group of 2D materials possessing various advantages such as high chemical stability, large surface area, hydrophilicity, tunable surface properties, ease of functionalization, and high electron kinetic rates.[19,20] $Ti_3C_2T_x$ MXenes have also been reported to be excellent detection platforms for constructing advanced sensors.[21] The etching of MXene yields MQDs having properties similar to the parent MXene, including interesting optical, electrical, and mechanical characteristics.[22] They also display good conductivity, water solubility, biocompatibility, edge effects, and unique quantum confinement, making them exciting candidates for electrochemical sensing applications.[23,24] They also have competent, plentiful surface-active sites, a higher surface-to-volume ratio than their parent material, and lateral dimension <10 nm.[25] Literature reports the successful detection of various biomolecules upon employment of MQDs.[25,26] These properties extend the applicability of MQDs in various fields, including photocatalytic, biomedical, fluorescence, electrochemical, and electrochemiluminescence applications.

In this study, we have reported the fabrication of a BNMQD-based electrode for crt quantification, as depicted in Scheme 1. The high electrical conductivity, abundant surface-active sites, and quantum confinement of the synthesized MQD promote the highly selective electrooxidation of crt. The fabricated electrode was calibrated under optimized conditions and applied toward crt detection in pharmaceutical formulations to explore its performance.

2. Materials and methods

2.1 Materials required

Ti_3AlC_2 MAX powder, lithium fluoride, HCl, H_2SO_4, HNO_3, NaOH, *p*-phenylene diamine, boric acid, methanol, $[Fe(CN)_6]^{3-/4-}$, KH_2PO_4, K_2HPO_4, and *N*-methyl-2-pyrrolidone were ordered from SD Fine Chemical Ltd, India. Phosphate buffered saline (PBS) prepared using KH_2PO_4 and K_2HPO_4 (pH 7.0) was employed for additional analysis. Crt was procured from Sigma-Aldrich.

2.2 Instrumentation

CV, DPV, and EIS studies were conducting using a CHI electrochemical workstation (model CHI608E). A three-electrode system was utilised for electrochemical investigations. A three-electrode system involving a reference electrode (saturated calomel electrode), a counter electrode (Pt foil), and a working electrode (fabricated CFP electrodes) was used. TEM images were taken using JEOL Japan, JEM-2100 Plus. XRD results were procured employing an X-ray diffractometer (Bruker AXS D8 Advance). A Kratos Axis Ultra X-ray photoelectron spectrometer was used to perform XPS studies to confirm

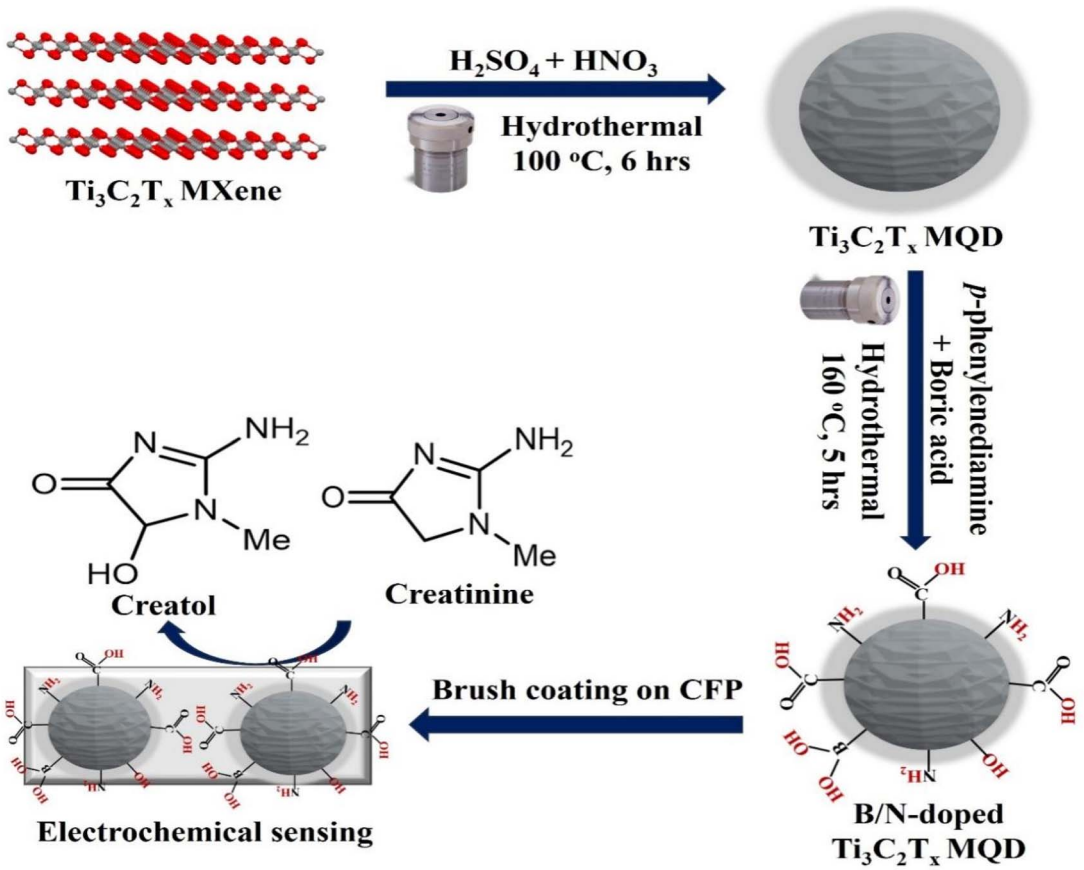

Scheme 1 Synthesis of the BNMQD composite for developing the BNMQD/CFP electrode for electrochemical crt detection.

the chemical environment and binding energy. Raman spectra of the MQDs were recorded employing a Lab RAM HR FT-Raman module with a laser source of 532 nM.

2.3 Preparation of sensor electrodes

2.3.1 Synthesis of $Ti_3C_2T_x$ MXene. A minimally intensive layer delamination (MILD) procedure was used to synthesise $Ti_3C_2T_x$ MXene from the MAX powder. One gram of lithium fluoride (LiF) was added to 20 ml of 6 M HCl. To this mixture, 1 g of Ti_3AlC_2 MAX phase was gradually introduced (10 minutes) with an ice-cold water bath to ensure proper dissipation of heat generated from an exothermic reaction. The solution was then continuously stirred at 500 rpm for 24 hours at 35 °C, followed by washing (with deionised water) to remove unreacted traces of HF acid. Further, the solution was then hand-shaken for 6 minutes, accompanied by centrifugation at 3500 rpm for 5 minutes until a dark-green supernatant (pH $\geq$ 5) was obtained. The precipitate consisting of $Ti_3C_2T_x$ MXene was then kept for over-drying.

2.3.2 Synthesis of $Ti_3C_2T_x$ MQDs. The $Ti_3C_2T_x$ MQDs were prepared by using the hydrothermal method. A total of 100 mg of $Ti_3C_2T_x$ MXene was added to a mixture of 30 ml H_2SO_4 and 10 ml HNO_3. The solution was transferred to a Teflon-coated hydrothermal vessel and placed in a muffle furnace at 100 °C for 6 hours. The white-coloured solution was poured into 100 ml of ice-cold water. Afterward, NaOH was introduced to regulate the pH to a level of 7.0, followed by centrifugation at 8000 rpm for 12 minutes and subsequent drying at 75 °C for 6 hours. A total of 40 mg of the synthesised MQDs was combined with 20 ml of distilled water and 10 ml of methanol. An amount of 20 mg of *p*-phenylene diamine and 20 mg of boric acid was introduced into this solution, followed by transfer to a Teflon-lined hydrothermal bomb and kept inside a muffle furnace for 5 hours at 160 °C. The resultant solution was red-coloured and subjected to centrifugation at 4000 rpm for 10 minutes, followed by subsequent drying at 80 °C for 6 hours to synthesise the BNMQDs. The B-doped and N-doped MQDs were synthesised by adding either 20 mg of *p*-phenylene diamine or 20 mg of boric acid, respectively, using the same procedure.

2.3.3 Preparation of BNMQD-based electrode. The synthesized MQDs, B-doped MQDs, N-doped MQDs, and BNMQDs were brush-coated on separate bare CFP electrodes. A mixture was made using NMP and PVDF. All the MQDs were mixed with this mixture to establish proper coating onto the CFP electrodes. A small dimension of 2 cm $\times$ 0.5 cm Toray CFP sheet was cut and pasted at the end of the copper wire using conducting ink and PTFE tape to ensure electrical conductivity. A total area of 0.50 cm^2 was further used for electrochemical studies.

2.4 Real samples preparations – tablets

The functional usability of the BNMQD/CFP was examined by applying pharmaceutical formulation prepared by grinding tablets and filtering through Whatman filter paper to remove contaminants. The prepared standard solutions were then used to study sensor performance using the standard addition method.

3. Results and discussion

3.1 Surface and structural morphology analysis

The BNMQDs were formed because the aromatic and amine groups in the *p*-phenylene diamine undergo condensation followed by polymerisation at elevated temperatures. The boron species in boric acid react with the nitrogen- and oxygen-containing groups, forming boronic esters incorporated into the MXene QDs in the form of boron dopants. The polymerised intermediates undergo further carbonisation and passivation, forming BNMQDs. The synthesised BNMQDs are quasi-spherical structures, possess a uniform size, and are well dispersed, as shown in Fig. 1a. The histogram shown in Fig. 1b displays that the sizes of BNMQDs are primarily distributed in the range of 5.0–9.5 nm. The mean lateral size was calculated as 7.76 nm by measuring 40 random quantum dots. The HRTEM image in Fig. 1c displays the crystalline characteristics of the obtained BNMQDs. In addition, the lattice fringe with an inner plane spacing was calculated to be 0.19 nm.

3.2 XRD

The XRD spectra for BMQD, NMQD and BNMQD show significant shifts when compared to the MQD spectra. The disappearance of an intense peak at 35° (2θ) ascribed to (104)

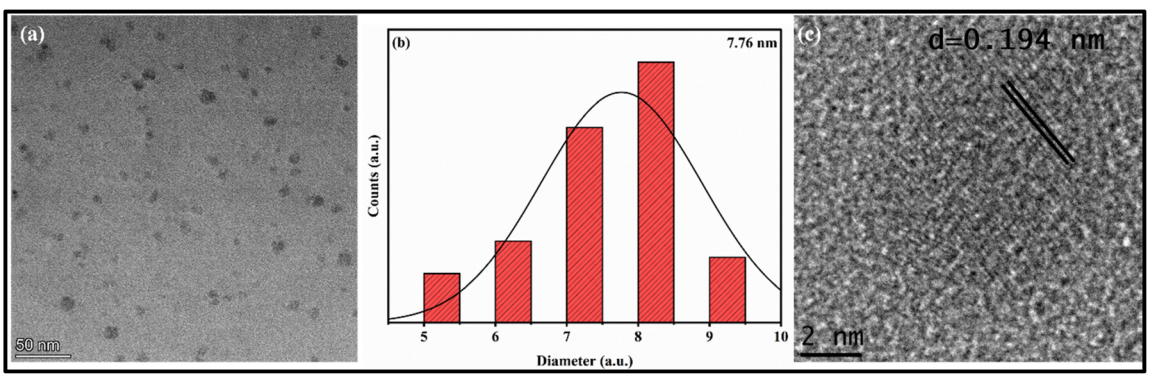

Fig. 1 (a) TEM image, (b) size distribution histogram, (c) HRTEM image of BNMQDs.

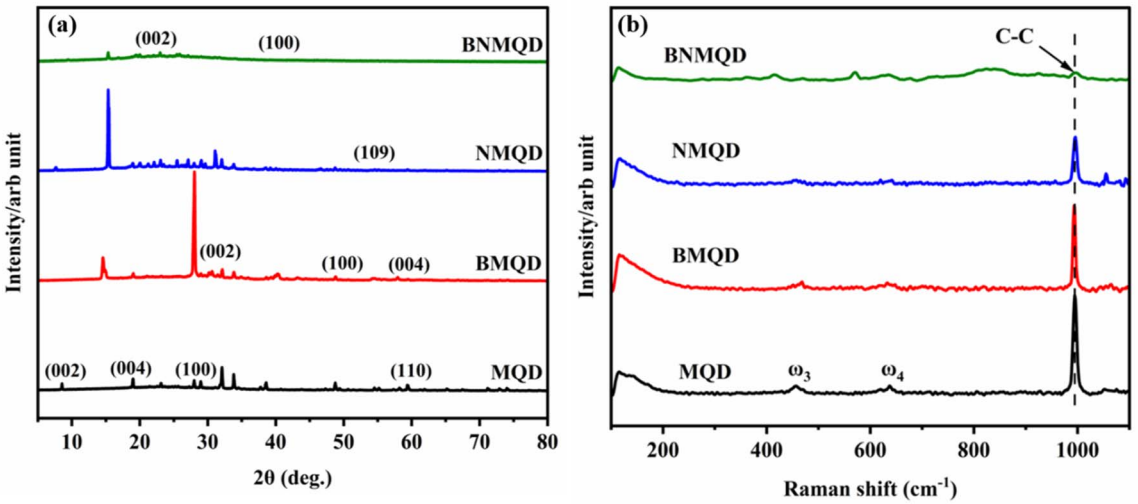

Fig. 2 (a) XRD patterns of MQDs, B-doped MQDs, N-doped MQDs, and BNMQDs. (b) Raman spectra of MQDs, B-doped MQDs, N-doped MQDs, and BNMQDs.

indicates the complete removal of the Al layer, as shown in (Fig. 2a).[27] The existence of the peak at 60° (2θ) related to (110) confirms the existence of a layered structure in the obtained MQDs.[28] The obtained XRD pattern of the $Ti_3C_2T_x$ MQDs shows an intense, broadened peak at 24° (2θ), depicting an amorphous nature similar to MQDs synthesised using the hydrothermal technique.[29] Also, a shift in (002) peak towards a lower angle than $Ti_3C_2T_x$ MXene was observed. This can be due to functional groups (–OH/=O/–F). The intense 19° (2θ) signal corresponds to the (004).[30] The N-doped MQDs demonstrate a broadened and less intense peak similar to $Ti_3C_2T_x$ MXene. An amorphous peak at 24° (2θ) corresponds to the carbon-rich structure.[31] The small peak at 33° (2θ) is consistent with the other reported works.[32] The peaks associated with N-doped MQDs are highly similar to $Ti_3C_2T_x$ MXene, substantiating the existence of a hexagonal crystal phase. However, a reduction in the particle size of N-doped MQDs can be understood by lowering the peak intensity.[33] Additionally, the minor shifts in the peak positions could be ascribed to the alteration in the electronic structure owing to the presence of N species, which is commonly reported in the literature.[34] The B-doped MQDs demonstrated unique peaks at 28.04° (2θ) associated with (002), 40.6° (2θ), and 43.4° (2θ) corresponding to (100), which are ascribed to the graphitic carbon cores of the synthesised MQDs.[35–37] Doping with B induces lattice expansion and causes a downshift of the XRD peak.[38] The peaks at 19.05° (2θ) and 59.7° (2θ) assigned to (800) and (004) confirm the surface functionalisation by boron atoms.[39] Cases involving co-doping with B and N were expected to increase both disorder and lattice distortion as per the previous reports.[40] The BNMQDs display two blunt and broad peaks at 24° (2θ) and 42° (2θ) corresponding to attributed to (002) and (100) planes, confirming the graphitic structure.

3.3 Raman analysis

Raman spectra of all the MQDs, B-doped MQDs, N-doped MQDs, and BNMQDs showed a broad peak near 1000 cm^{-1} analogous to the C–C vibrations (Fig. 2b).[41] Also, only the ω_3 and ω_4 peaks around 450 and 630 cm^{-1} were present in the $Ti_3C_2T_x$ MQDs. The disappearance of ω_1 and ω_2 peaks present in Ti_3AlC_2 MAX phase confirms the removal of Al in the synthesised $Ti_3C_2T_x$ MQDs.[42,43] The B-doped MQDs displayed various Raman peaks between 100 and 800 cm^{-1}, attributed to different termination groups in $Ti_3C_2T_x$. The observed peaks in the given range were identified as 206, 290, 387, 434, 583, 633, and 721 cm^{-1}.[43]

3.4 FTIR

The FTIR spectra of MQDs, B-doped MQDs, N-doped MQDs, and BNMQDs were analysed to substantiate the synthesis of all MQD-based QDs, as described in Fig. 3. The adsorption maximum at 3325 cm^{-1} aligns with the stretching and bending

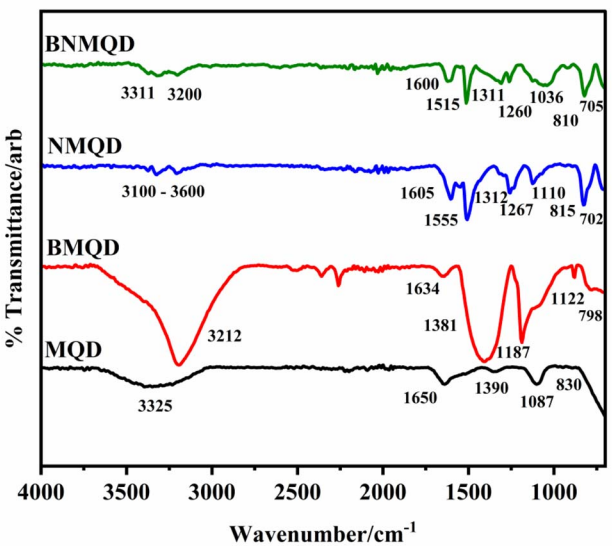

Fig. 3 FTIR spectra of MQDs, B-doped MQDs, N-doped MQDs, and BNMQDs.

vibration of the –OH group.[44] The 1650 cm^{-1} peak in $Ti_3C_2T_x$ MQDs corresponds to the C–O/C=O group.[31] The 1390 and 1087 cm^{-1} peaks are attributed to the O–H and C–F groups. The shoulder peaks at 830 cm^{-1} could be due to the Ti–F bonding stretching vibration.[45] The absorption maximum around 3212 cm^{-1} corresponds to O–H bonds.[46] The peaks at 1634 and 1386 cm^{-1} substantiate the presence of the COO– group.[47] The peak at 1122 cm^{-1} is associated with the C–B bond.[48] Moreover, the B–C stretching frequency appeared at 1190 cm^{-1}.[49] The vibration of epoxy groups showed a small peak around 798 cm^{-1}.[50] In the case of N-doped MQDs, the broad peak at 3310 cm^{-1} corresponds to O–H stretching vibrations of carboxylic acid.[51] The 3249 cm^{-1} peak corresponds to the stretching modes of C–N and N–H, confirming the existence of amino-containing functional groups.[52] The absorption band around 1600 cm^{-1} is due to the N–H bonds, substantiating the successful synthesis of N-containing groups.[53] The peaks around 1515 cm^{-1} and 1260 cm^{-1} are also attributed to the N–H and C–N bond vibrations.[54] A small peak corresponding to the bending vibration of the C–O–C bond occurred at 1311 cm^{-1}.[55] The peaks at 810 cm^{-1} and 705 cm^{-1} correspond to the wagging vibrations of NH_2 and $-CH_2$ functional groups.[56,57] The absorption maximum of around 3100–3600 cm^{-1} correlates with the stretching vibrations of N–H and O–H.[58] The peaks at 1605 cm^{-1} and 1555 cm^{-1} confirm the existence of a C=C.[59,60] The 1347 and 1267 cm^{-1} peaks are attributed to the B–N and C–O–C bonds.[61] The absorption peak at 1120 cm^{-1} is attributed to the B–C stretching in BNMQDs.[62] The peak at 815 cm^{-1} confirms the existence of a B–N bond.[63] The N–H scissoring mode was established due to a peak at 702 cm^{-1}, substantiating the existence of a primary amine.[64]

3.5 XPS analysis

XPS analysis provides an overall description of the chemical constituents of the BNMQDs, as shown in Fig. 4. The existence of C, Ti, N, O, B, and F in the BNMQD/CFP was substantiated by the six distinct and strong peaks observed in the survey scan. The C 1s spectra after deconvolution resulted in four peaks at 284.4, 285.2, 286.0, 288.0, confirming the existence of C–C, C–OH, C–N, and C–Ti groups, and thereby confirming the successful synthesis of BNMQD/CFP (Fig. 4a).[65–68] Upon deconvolution, the Ti 2p spectra resulted in four significant peaks at 460.7, 461.2, 461.7, and 467.1 eV, corresponding to Ti–O, Ti $2p_{3/2}$, C–Ti^{2+} ($2p_{1/2}$), and Ti $2p_{1/2}$ (Fig. 4b).[69–72] The peak at 530.18 eV confirmed the presence of the OH–Ti/C group. In N 1s spectra, the characteristic peaks at 399.1, 400.5, and 401.8 eV are analogous to N–H, N–$(C)_3$, and N–C. This substantiates the presence of nitrogen, which could result in increased quantum yield (Fig. 4c).[73] The presence of N–O, C–O, and C=O bonds was confirmed by the peaks at 531.0, 531.6, and 531.9 eV, respectively (Fig. 4d).[74–76] The deconvolution of B 1s gave rise to four peaks at 185.2, 191.4, 195.7, and 198.2 eV, confirming the presence of elemental boron, B–N, B–F, and B–N_3 (Fig. 4e).[77–80] The F 1s spectra exhibited peaks at 686.8, 685.2, and 684.4 eV, consistent with F–C, C–Ti–F_x, and F–Ti (Fig. 4f). The observed peaks also correlated with the C 1s and Ti 2p spectra.[81] When XPS was recorded post crt oxidation, the C 1s and O 1s spectra displayed similar peaks for C–OH and C–N, C–Ti, C=O, N–O, C–O, and C=O bonds, respectively. This confirms that the oxidation of crt is solely dependent on electrooxidation and not due to the chemical oxidation in the presence of functional groups such as C=O and COO^- (Fig. S1).

3.6 Electrochemical studies

3.6.1 Electrochemical properties of developed electrodes. The electrodes' electrochemically active surface area (ECSA) was analysed and compared by determining the electrical double-layer capacitance (C_{dl}). CV curves were swept in a non-faradaic region, wherein the scan rates were varied from 10 mV s^{-1} to 500 mV s^{-1}, as described in Fig. 5. The formula used to calculate the ECSA value of the electrodes is as follows:

$$\mathrm{ECSA} = (C_{dl}/C_s) \times S$$

Where C_s is the specific capacitance of the electrode (for pristine CFP, C_s = 0.0011 F cm^{-2}),[82] and S is the surface area of the electrode.

Since C_{dl} and ECSA are directly proportional, a higher C_{dl} value implies more catalytically active centres on the electrode surface. Notably, the C_{dl} value achieved for BNMQD was significantly higher (18.6 mF cm^{-2}) when compared to NMQD (15 mF cm^{-2}), BMQD (8 mF cm^{-2}) and MQD (4 mF cm^{-2}), which can be attributed to its excellent adsorption capacity for the electroactive intermediates over the electrode surface. This amplified performance suggests that the doping of B- and N-atoms plays a crucial role in generating additional active sites, thereby enhancing the catalytic efficiency of the electrode.

EIS is used to assess the transference of electrons, kinetic barriers, and variations in the interfacial electrocatalytic characteristics of the developed electrodes.[83] It is a practical, effective, and non-destructive electrochemical technique for measuring the surface properties of the developed sensors. Nyquist plots were utilised to analyse the data obtained from electrochemical impedance results by fitting them to Randles' equivalent circuit. The various components of Randles' equivalent circuit include charge transfer (R_{ct}), electrolyte solution resistance (R_s), and double-layer capacitance (C_{dl}). The R_{ct} value depends upon the adsorption behaviour demonstrated by the modified electrode, which can be calculated from the semi-circular diameter. R_{ct} influences the electron transfer kinetics occurring at the electrode surface. For this, utilising the three-electrode system, bare, MQD, BMQD, NMQD, and BNMQD/CFP electrodes were tested at 0.05 V s^{-1} in 0.1 M KCl (supporting electrolyte) consisting of 5 mM redox mediator, with the obtained EIS measurement parameters depicted in Table 1. The R_{ct} value for the bare CFP electrode was the highest (804.9 Ω) owing to poor electrical conductivity, as depicted in Fig. 6b. Upon modification with MQDs, the R_{ct} value notably dropped to 537.0 Ω. This was attributed to the presence of several surface-active sites of the MQDs. BMQD and NMQD/CFP electrodes demonstrated R_{ct} values of 352.12 Ω and 275.79 Ω, respectively. Interestingly, upon modification with both B and N for the BNMQD/CFP electrode, the least R_{ct} value (87.0 Ω) was obtained,

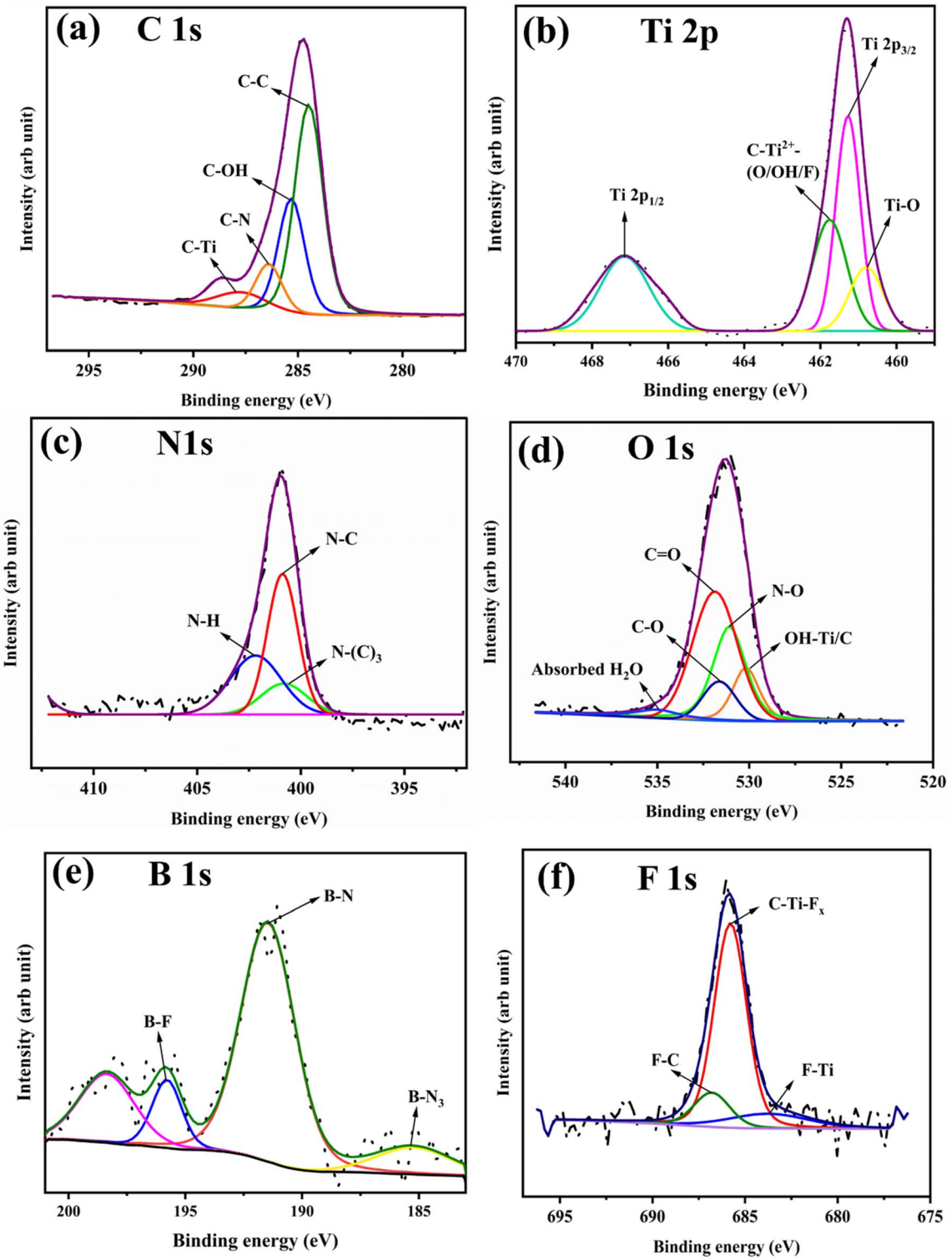

Fig. 4 (a–f) XPS analysis of the BNMQD/CFP electrode before oxidation of crt. The obtained XPS spectrum is shown with a dotted line.

owing to the higher surface area, improved electron transfer ability, and synergistic effect between the doped B and N atoms, leading to enhanced electron transference occurring on the BNMQD/CFP electrode surface.

The electrochemical activity and electron transferability of the bare, MQD, BMQD, NMQD, and BNMQD/CFP electrodes were tested using the CV technique in the same solution employed for EIS within the potential range of −0.1 to 1.0 V at 0.05 V s^{-1}. The bare CFP electrode exhibited well-separated redox peaks with minimal electrical conductivity (Fig. 6a). Upon modification with MQD, BMQD, and NMQD, the redox peaks were less split (minor shift), which improved the

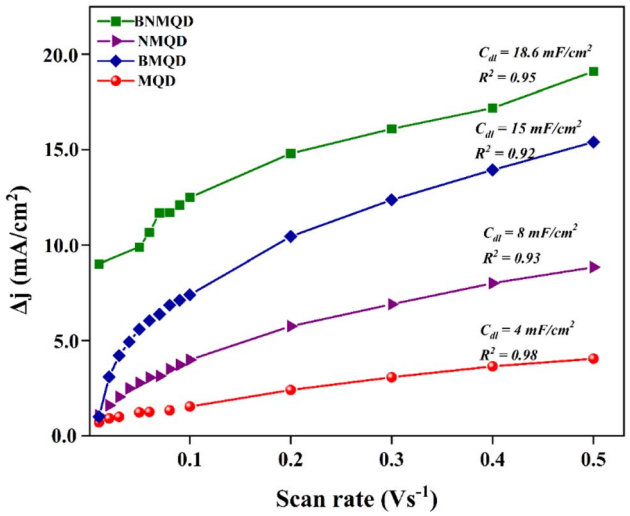

Fig. 5 Plot of Δ*j versus* the scan rate for the modified electrodes; the slope of the linear fitted line corresponds to the C_{dl} values.

Table 1 EIS measurement parameters used for the Nyquist plots of different modified electrodes[a]

Electrode	Initial potential	R_1	R_2	C
Bare CFP	0.132	25.95	780	3.985×10^{-5}
MQD	0.215	36.61	502	2.229×10^{-5}
BMQD	0.126	35.73	319.1	5.017×10^{-5}
NMQD	0.438	35.03	243.3	3.217×10^{-5}
BNMQD	0.08	19.7	67.12	1.555×10^{-7}

[a] Frequency range: 1 Hz to 1×10^5 Hz, amplitude = 0.005.

redox peak current values. The finally modified electrode (BNMQD) demonstrated the minor peak-to-peak separation and maximum redox current peaks, owing to the rapid electron-transfer kinetics, heightened surface area, and electrostatic interactions between the BNMQD/CFP and the redox mediator.

3.6.2 Electrochemical performance of modified electrodes towards crt. The electrocatalytic sensing performance of bare, MQD/CFP, BMQD/CFP, NMQD/CFP, and BNMQD/CFP electrodes towards 100 μM crt sensing in 0.1 M PBS (pH 7) at 0.05 V s^{-1} is displayed in Fig. 7a. The electrooxidation mechanism of crt on the BNMQD/CFP electrode is depicted in Fig. 7b. The bare CFP electrode displayed a weak, broad anodic peak current of 2.501×10^{-5} A cm^{-2} at 0.58 V for crt electrooxidation. On modifying the bare CFP electrode with MQD, BMQD, and NMQD, a significant increase in anodic peak current values (6.304×10^{-4}, 1.014×10^{-3}, and 1.856×10^{-3} A cm^{-2}) was observed, along with a negative shift in potential values compared to the bare CFP electrode. The BNMQD/CFP electrode displayed a significantly lower anodic potential (0.50 V) and the highest current peak (2.747×10^{-3} A cm^{-2}) for crt sensing. This could be attributed to the several surface-active sites, a large surface area, several diffusion pathways, high electrical conductivity, and the synergistic effect between the doped B and N atoms. Therefore, BNMQD/CFP is a promising electron transfer mediator as it accelerates the anodic oxidation of crt.

3.7 Buffer pH effect on crt detection

The pH of the supporting electrolyte (PBS) is a crucial parameter because it influences the redox behavior associated with electroactive species. The pH range was adjusted to improve the developed sensor's electrochemical sensing performance and sensitivity. In this work, the sensing ability of the developed electrode was affected by the change in the electrolyte pH, with essential roles played by both protons and electrons. The pH range was optimized within 5.0–10.0 for 100 μM crt detection in 0.1 M PBS at 0.05 V s^{-1}, as depicted in Fig. S2a. The electrooxidation process fluctuated in response to the protonation/deprotonation reactions. The anodic current response was enhanced with an increase in pH (5.0–7.0), followed by a decrease with a further increase in pH (7.0–10.0). pH 7.0 was selected for further electrochemical studies because it exhibited the highest anodic current response and is eminently close to the biological pH for greater practical applicability. Also, the

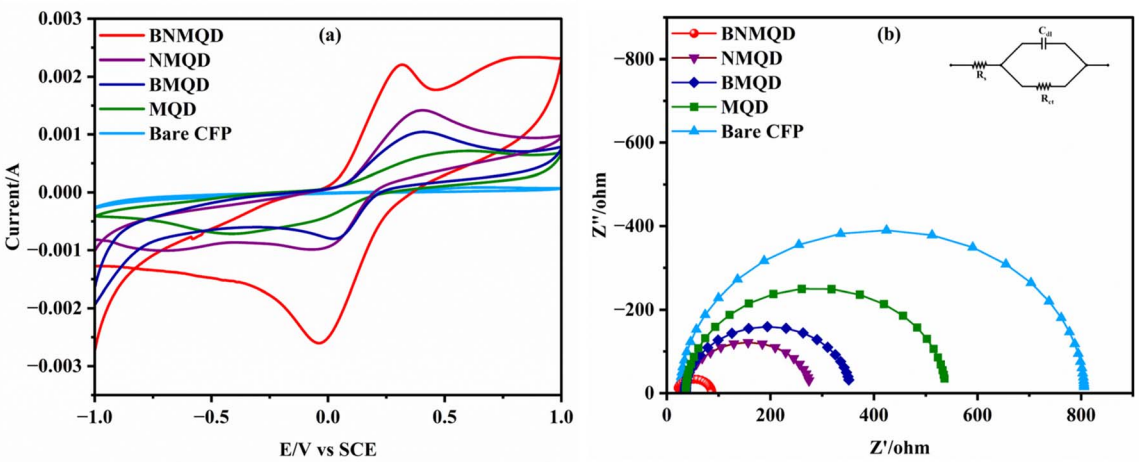

Fig. 6 (a) CV curves and (b) Nyquist plots of bare and modified electrodes in a 5 mM redox mediator and 0.1 M KCl solution.

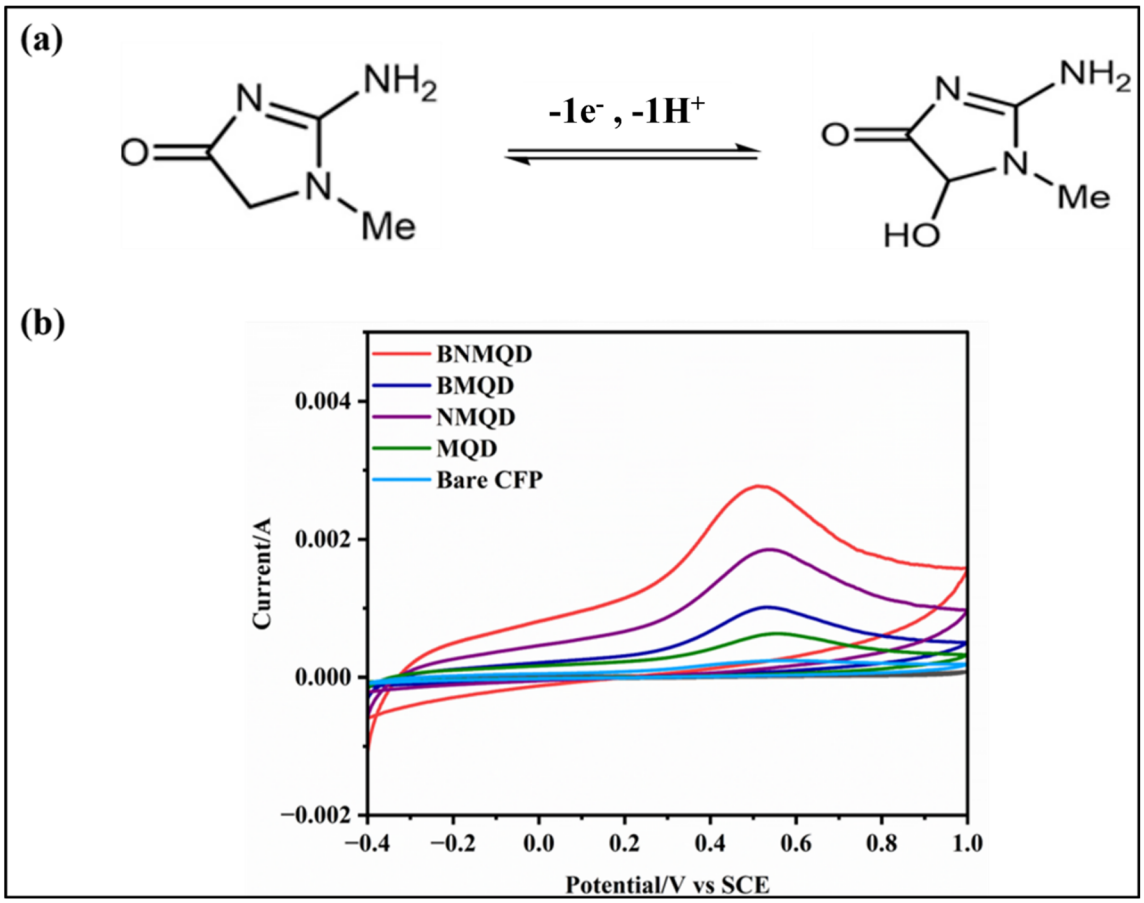

Fig. 7 (a) Electrooxidation mechanism of crt. (b) CV of electrooxidation of 100 μM crt at the bare CFP, MQD/CFP, BMQD/CFP, NMQD/CFP, and BNMQD/CFP electrodes.

negative shift in peak value indicates the influence of pH variations, proton, and electron transference on the crt oxidation. The linear relation between the peak potential and pH has been shown in Fig. S2b and eqn (1).

$$\text{For crt: } E_p = -0.05529\ \text{pH} + 0.85381\ (R^2 = 0.99847) \quad (1)$$

As per Nernst equation, the peak potential and pH (eqn (2)) can be related as follows:

$$E\ (\text{V}) = E_0 - 2.303RT/F\ (m/n)\ \text{pH} = E_0 - 0.059\ (m/n)\ \text{pH} \quad (2)$$

Herein, m and n represent the number of transferred H^+ and e^-, respectively. The linear slope value of crt 0.05529 V pH^{-1}, is near the Nernstian value (0.0592 V pH^{-1}), substantiating the equal involvement of H^+ and e^- during crt electrooxidation.

3.8 Optimization of reaction mechanism

The scan rate significantly influences the electrocatalytical efficiency and behavior associated with the fabricated electrode. The BNMQD/CFP sensor was tested using CV with a scan rate gradually increasing from 0.01 to 0.10 V s^{-1} to understand the reaction mechanism, as demonstrated in Fig. 8a. On plotting the scan rate against the current graph, a linear variation with increasing scan rate was observed, with $R^2 = 0.99694$, which is apparent in the occurrence of an adsorption-controlled mechanism as depicted in Fig. 8b.[84] The increased anodic peak current is primarily a result of surface absorption of crt.

The corresponding regression eqn (3) obtained is as follows:

$$i_p\ (\text{A}) = 0.0161\ \text{V} - 0.00263\ (R^2 = 0.99694). \quad (3)$$

The following equation was employed to determine the no. of e^- participating in the reaction mechanism (eqn (4)):

$$E_p - E_{p/2} = 0.0564/n \quad (4)$$

The 'n' was determined to be 1.06, equivalent to 1, thereby confirming the participation of $1H^+$ and $1e^-$ for crt electrooxidation.

3.9 Analytical performance

DPV is more sensitive to changes in the faradaic current, provides better peak resolution and technique compared to CV, and exhibits reduced background current density. It is also helpful in the quantification of analytes, even at low concentrations. DPV was employed to ascertain crt under optimal environment utilizing the BNMQD/CFP electrode. The anodic

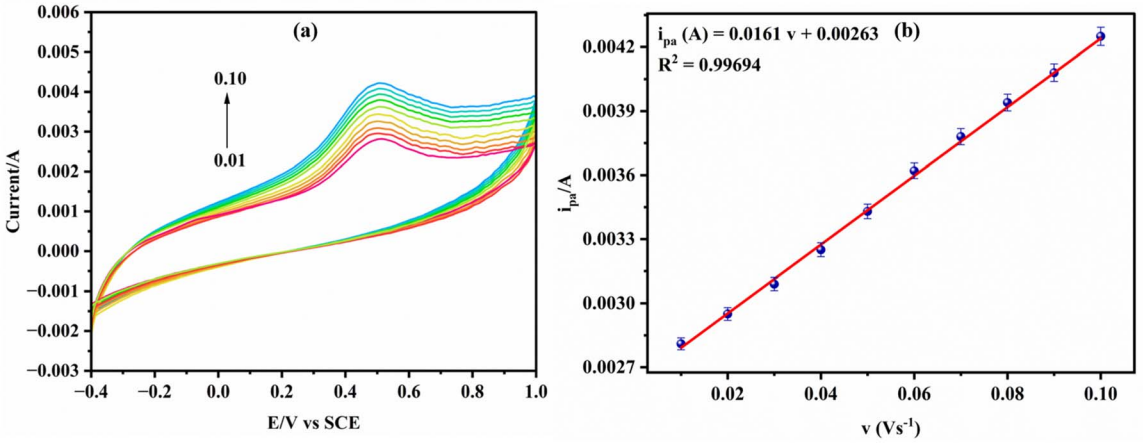

Fig. 8 (a) CV responses of 100 μM crt at the BNMQD/CFP electrode at varying scan rates. (b) Correlation between current response and varying scan rate.

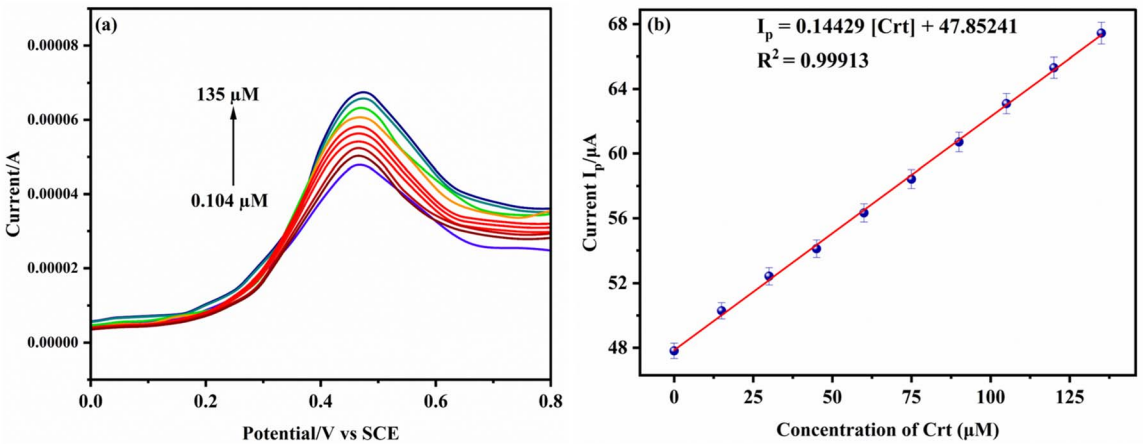

Fig. 9 (a) DPV responses of the BNMQD/CFP sensor at increasing crt concentrations. (b) Calibration plot of crt using the BNMQD/CFP sensor.

current peaks were obtained for the different crt concentrations in 0.1 M PBS (pH 7) within (0–0.8 V), as displayed in Fig. 9a. As the concentration of crt increased, the anodic peak current showed a linear increase at 0.47 V. This validates the usefulness of the BNMQD/CFP sensor in determining crt at low concentrations.

A linear equation (eqn (5)) along with regression coefficient obtained from the calibration curve, as demonstrated in Fig. 9b, is given as follows:

$$I_p\ (\mathrm{A}) = 0.14429\ [\mathrm{crt}] + 47.85241\ (R^2 = 0.99913) \quad (5)$$

The LOD and LOQ values of the developed BNMQD/CFP sensor, calculated using the formulae LOD = $3.3\sigma/S$ and LOQ = $10\sigma/S$, were found to be 34.53 nM and 104.65 nM, respectively. The wide linear range for the developed BNMQD/CFP sensor was calculated as 0.104–135 μM. Table 2 evaluates the electroanalytical performance of the fabricated sensor by analyzing its LOD, LOQ, and detection range in comparison with those reported in the literature.

Table 2 Different analytical parameters for crt sensing using various reported sensors

Electrode material	Linear range (μM)	LOD (μM)	Ref.
Fe_3O_4-NPs/CHIT-*g*-PANI	1–800	1	85
c-MWCNT/PANI composite film	10–750	0.1	86
ZnO-NPs/CHIT/c-MWCNT/PANI composite film	10–650	0.5	87
Cu/screen printed carbon electrodes (SPCE)	6–378	0.0746	88
(PEI/PTA)20 film electrode	0.125 to 62.5	0.06	89
BNMQD/CFP	0.104–135	0.034	Present work

3.10 Selectivity of the BNMQD/CFP sensor

Studying the interference and selectivity of the modified electrode is an essential feature for practical applications. Since most interferents co-exist with similar functional groups and sizes, achieving high selectivity among the common interfering species at physiological concentrations is of paramount interest. Therefore, DPV was employed to study the selectivity of the BNMQD/CFP sensor for crt quantification (50 μM) in the presence of a 15-fold concentration of commonly interfering species, including glucose, DA, UA, and AA, as demonstrated in Fig. 10a–d. The results demonstrated the specific selectivity of the BNMQD/CFP sensor for crt (50 μM), as the anodic peak potential and anodic current values did not vary upon adding interferents. The addition of interferents had a negligible effect on crt, as it did not hamper the specific oxidation of crt. These findings result from an optimal electrocatalytic environment generated by the synergistic effect between the BNMQD/CFP and crt. The aromatic groups of crt bonded with the BNMQD/CFP sensor surface owing to stable electrostatic interactions, leading to accelerated specific oxidation of crt. Therefore, the fabricated BNMQD/CFP sensor can detect crt precisely. However, upon the addition of high concentration of various other interferents, including glycine, lactic acid, KNO_3, and Na_2CO_3, a slight shift in the crt potential was observed and can be considered a limitation. Comprehensive selectivity evaluation in complex biological samples remains a limitation of the present study and will be addressed in future investigations.

3.11 Real sample analysis

To examine the viability of the developed sensor for crt detection, the sensor was operated in the potential range of 0–0.8 V in 0.1 M PBS (pH 7) using the DPV technique with the standard addition method (SAM). Various known concentrations of the standard crt solution were added to the made-up pharmaceutical sample solution to estimate the recovery percentage. This resulted in an anodic peak of crt at 0.47 V in the prepared pharmaceutical-based real samples, as depicted in Table 3. The notable performance of the reported sensor was confirmed by the recovery percentage (96–100.3%). While the present study shows the efficacy of the developed method using pharmaceutical formulations, future work is expected to extend the application to biological matrices such as blood, serum, or urine. This will enable a deeper understanding of the methodology under clinically relevant conditions.

3.12 Reproducibility, repeatability, and stability studies of BNMQD/CFP

Studying the fabricated sensor's reproducibility, repeatability, and stability standards is paramount in biomarker detection applications. Five repetitive studies using BNMQD/CFP electrodes were conducted to assess reproducibility by comparing

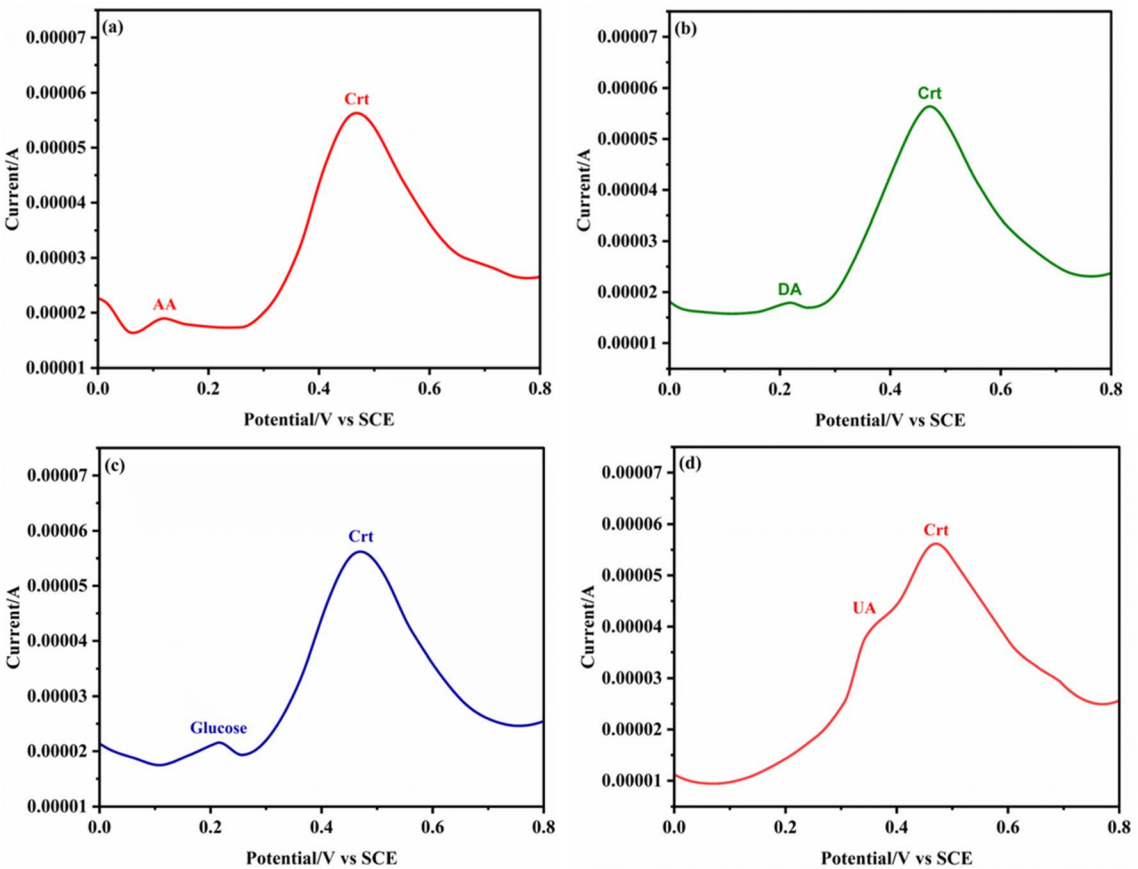

Fig. 10 DPV responses for 50 μM crt in the presence of 750 μM (a) AA, (b) DA, (c) glucose, and (d) UA.

Table 3 Quantification of crt levels in two different pharmaceutical formulations using BNMQD/CFP in 0.1 M PBS (pH 7)

Sample	Concentration (expected) (μM)	Concentration (added) (μM)	Concentration (observed) (μM)	Recovery %	[a]RSD %
Crt (A)	10.0	0.0	9.99	99.9	0.99
		5.0	14.97	99.7	0.98
		10.0	19.95	99.4	0.96
		20.0	29.98	99.8	0.97
Crt (B)	20.0	0.0	19.97	99.7	0.98
		5.0	24.96	99.6	0.96
		10.0	29.98	99.8	0.98
		20.0	39.97	99.7	0.98

[a] Mean value of three determinations.

their anodic current responses. The attainment of an RSD value of 1.15% with 100 μM crt implies high reproducibility of the developed sensor, as shown in Fig. S3a. A series of ten measurements (100 μM crt) resulted in an RSD value of 1.18%, demonstrating high repeatability of the BNMQD/CFP, as observed in Fig. S3b. Finally, the BNMQD/CFP electrode was preserved in the fridge at 5 °C for five weeks for the persistent stability studies. The anodic current responses for these stored electrodes were then measured, retaining 96%, which demonstrated remarkable current responses towards crt detection (Fig. S3c).

4. Conclusions

In the present work, MQDs and B- and N-doped MQDs were synthesized by the MILD method to obtain $Ti_3C_2T_x$ MXene, followed by hydrothermal synthesis of MQDs. The developed BNMQD/CFP sensor demonstrated outstanding electrocatalytic performance towards crt oxidation. The heightened analytical ability of the BNMQDs can be attributed to the surface-active sites resulting in rapid movement of the electrolyte ions during electrochemical oxidation and the synergistic effect between the doped B and N atoms present in the BNMQDs. The BNMQD/CFP sensor could detect crt from 0.104 to 135 μM with an LOD of 34.53 nM and an LOQ of 104.65 nM. The sensor demonstrated remarkable stability, repeatability, and reproducibility under optimal conditions. Also, there was high selectivity for crt detection in the presence of closely interfering species with similar physiological concentrations and structures.

Author contributions

Rijo Rajeev: conceptualization, methodology, formal analysis, investigation, writing – original draft. Ann Mariella: methodology, formal analysis, investigation. Anitha Varghese: conceptualization, investigation, supervision, writing – review & editing.

Conflicts of interest

The authors declare that they have no known competing financial interests or personal relationships that could have appeared to influence the work reported in this paper.

Data availability

All data supporting the findings of this study are available within the article.

Supplementary information is available. See DOI: https://doi.org/10.1039/d5ra04474j.

Acknowledgements

The authors thank Christ University and CeNS for providing the necessary facilities to conduct this work.

References

1 F. F. Fazial, L. L. Tan and S. I. Zubairi, *Sens. Actuators, B*, 2018, **269**, 36–45.
2 E. P. Randviir and C. E. Banks, *Sens. Actuators, B*, 2013, **183**, 239–252.
3 M. M. Erenas, I. Ortiz-Gómez, I. De Orbe-Payá, D. Hernández-Alonso, P. Ballester, P. Blondeau, F. J. Andrade, A. Salinas-Castillo and L. F. Capitán-Vallvey, *ACS Sens.*, 2019, **4**, 421–426.
4 K. Kaur, M. Kataria, M. Kaur, A. K. Sood, M. Kumar and V. Bhalla, *ACS Sustain. Chem. Eng.*, 2019, **7**, 14829–14833.
5 X. Gao, R. Gui, H. Guo, Z. Wang and Q. Liu, *Sens. Actuators, B*, 2019, **285**, 201–208.
6 B. Babamiri, A. Salimi, R. Hallaj and M. Hasanzadeh, *Biosens. Bioelectron.*, 2018, **107**, 272–279.
7 R. Rajamanikandan and M. Ilanchelian, *Anal. Methods*, 2018, **10**, 3666–3674.
8 A. Diouf, S. Motia, N. El Alami El Hassani, N. El Bari and B. Bouchikhi, *J. Electroanal. Chem.*, 2017, **788**, 44–53.
9 Y. Chen, G. Shen, R. Zhang, J. He, Y. Zhang, J. Xu, W. Yang, X. Chen, Y. Song and Z. Abliz, *Anal. Chem.*, 2013, **85**, 7659–7665.
10 C. Slot, *Scand. J. Clin. Lab. Invest.*, 1965, **17**, 381–387.
11 N. Zahoor, U. Danilenko and H. W. Vesper, *Clin. Mass Spectrom.*, 2019, **11**, 1–7.
12 R. Stosch, A. Henrion, D. Schiel and B. Guttler, *Anal. Chem.*, 2005, **77**, 7386–7392.
13 S. Hanif, P. John, W. Gao, M. Saqib, L. Qi and G. Xu, *Biosens. Bioelectron.*, 2016, **75**, 347–351.

14 A. M. Fekry, S. A. Abdel-Gawad, R. H. Tammam and M. A. Zayed, *Measurement*, 2020, **163**, 107958.
15 I. Pandey, P. K. Bairagi and N. Verma, *Sens. Actuators, B*, 2018, **277**, 562–570.
16 J. Xue, C. Han, Y. Yang, S. Xu, Q. Li, H. Nie, J. Qian and Z. Yang, *Inorg. Chem.*, 2023, **62**, 3288–3296.
17 Q. Huang, Y. Xu, Y. Guo, L. Zhang, Y. Hu, J. Qian and S. Huang, *Carbon*, 2022, **188**, 135–145.
18 B. Shao, Z. Liu, G. Zeng, H. Wang, Q. Liang, Q. He, M. Cheng, C. Zhou, L. Jiang and B. Song, *J. Mater. Chem. A*, 2020, **8**, 7508–7535.
19 M. Naguib, M. Kurtoglu, V. Presser, J. Lu, J. Niu, M. Heon, L. Hultman, Y. Gogotsi and M. W. Barsoum, *Adv. Mater.*, 2011, **23**, 4248–4253.
20 R. Rajeev, D. A. Thadathil and A. Varghese, *Crit. Rev. Solid State Mater. Sci.*, 2023, **48**, 580–622.
21 R. Rajeev, A. R. Cherian, D. A. Thadathil and A. Varghese, *Mater. Res. Bull.*, 2024, **169**, 112523.
22 A. M. B. Sariga, S. Kumar, R. Rajeev, D. A. Thadathil and A. Varghese, *Adv. Mater. Interfaces*, 2023, **10**, 2202139.
23 C. Chen, M. Boota, P. Urbankowski, B. Anasori, L. Miao, J. Jiang and Y. Gogotsi, *J. Mater. Chem. A*, 2018, **6**, 4617–4622.
24 M. Safaei and M. R. Shishehbore, *J. Mater. Sci.*, 2021, **56**(32), 17942–17978.
25 W. Luo, H. Liu, X. Liu, L. Liu and W. Zhao, *Colloids Surf., B*, 2021, **201**, 111631.
26 Y. Liu, S. Huang, J. Li, M. Wang, C. Wang, B. Hu, N. Zhou and Z. Zhang, *Microchim. Acta*, 2021, **188**, 1–12.
27 S. Yang, P. Zhang, F. Wang, A. G. Ricciardulli, M. R. Lohe, P. W. M. Blom and X. Feng, *Angew. Chem.*, 2018, **130**, 15717–15721.
28 O. Mashtalir, K. M. Cook, V. N. Mochalin, M. Crowe, M. W. Barsoum and Y. Gogotsi, *J. Mater. Chem. A*, 2014, **2**, 14334–14338.
29 T. Li, L. Yao, Q. Liu, J. Gu, R. Luo, J. Li, X. Yan, W. Wang, P. Liu, B. Chen, W. Zhang, W. Abbas, R. Naz and D. Zhang, *Angew. Chem., Int. Ed.*, 2018, **57**, 6115–6119.
30 M. Naguib, M. Kurtoglu, V. Presser, J. Lu, J. Niu, M. Heon, L. Hultman, Y. Gogotsi and M. W. Barsoum, *Adv. Mater.*, 2011, **23**, 4248–4253.
31 Q. Xue, H. Zhang, M. Zhu, Z. Pei, H. Li, Z. Wang, Y. Huang, Y. Huang, Q. Deng, J. Zhou, S. Du, Q. Huang and C. Zhi, *Adv. Mater.*, 2017, **29**, 1604847.
32 Q. Xu, L. Ding, Y. Wen, W. Yang, H. Zhou, X. Chen, J. Street, A. Zhou, W. J. Ong and N. Li, *J. Mater. Chem. C*, 2018, **6**, 6360–6369.
33 W. Huang, J. Liu, B. Bai, L. Huang, M. Xu, J. Liu, H. Rong and J. Zhang, *Nanotechnology*, 2018, **29**, 125606.
34 Y. Wang, Y. Wang, D. Liu, Y. Feng, D. Yang, S. Wu, H. Jiang, D. Wang and S. Bi, *Materials*, 2024, **17**, 6163.
35 V. Arul, P. Chandrasekaran, G. Sivaraman and M. G. Sethuraman, *Mater. Res. Bull.*, 2023, **162**, 112204.
36 X. Zhang, Y. Ren, Z. Ji and J. Fan, *J. Mol. Liq.*, 2020, **311**, 113278.
37 H. K. Sadhanala, S. Pagidi and A. Gedanken, *J. Mater. Chem. C*, 2021, **9**, 1632–1640.
38 N. Sohal, B. Maity and S. Basu, *RSC Adv.*, 2021, **11**, 25586–25615.
39 J. Vinoth Kumar, V. Arul, R. Arulmozhi and N. Abirami, *New J. Chem.*, 2022, **46**, 7464–7476.
40 H. L. Tran, W. Darmanto and R. A. Doong, *Nanomaterials*, 2020, **10**, 1883.
41 Q. Guan, J. Ma, W. Yang, R. Zhang, X. Zhang, X. Dong, Y. Fan, L. Cai, Y. Cao, Y. Zhang, N. Li and Q. Xu, *Nanoscale*, 2019, **11**, 14123–14133.
42 X. Chen, X. Sun, W. Xu, G. Pan, D. Zhou, J. Zhu, H. Wang, X. Bai, B. Dong and H. Song, *Nanoscale*, 2018, **10**, 1111–1118.
43 M. Naguib, M. Kurtoglu, V. Presser, J. Lu, J. Niu, M. Heon, L. Hultman, Y. Gogotsi and M. W. Barsoum, *Adv. Mater.*, 2011, **23**, 4248–4253.
44 Q. Zhang, Y. Sun, M. Liu and Y. Liu, *Nanoscale*, 2020, **12**, 1826–1832.
45 Y. Qin, Z. Wang, N. Liu, Y. Sun, D. Han, Y. Liu, L. Niu and Z. Kang, *Nanoscale*, 2018, **10**, 14000–14004.
46 L. Yang, Q. Zhang, Y. Huang, C. Luo, Z. Quan, H. Li, S. Sun and Y. Xu, *J. Colloid Interface Sci.*, 2023, **632**, 129–139.
47 L. Zhang, Z. Y. Zhang, R. P. Liang, Y. H. Li and J. D. Qiu, *Anal. Chem.*, 2014, **86**, 4423–4430.
48 J. Jana, M. Ganguly, K. R. S. Chandrakumar, G. M. Rao and T. Pal, *Langmuir*, 2017, **33**, 573–584.
49 V. Arul, P. Chandrasekaran, G. Sivaraman and M. G. Sethuraman, *Mater. Res. Bull.*, 2023, **162**, 112204.
50 X. Xu, T. Yuan, Y. Zhou, Y. Li, J. Lu, X. Tian, D. Wang and J. Wang, *Int. J. Hydrogen Energy*, 2014, **39**, 16043–16052.
51 A. Paul and M. Kurian, *Mater. Today Proc.*, 2020, **25**, 213–217.
52 B. B. Campos, C. Abellán, M. Zougagh, J. Jimenez-Jimenez, E. Rodríguez-Castellón, J. C. G. Esteves da Silva, A. Ríos and M. Algarra, *J. Colloid Interface Sci.*, 2015, **458**, 209–216.
53 R. Das, S. Parveen, A. Bora and P. K. Giri, *Carbon*, 2020, **160**, 273–286.
54 X. Ma, S. Li, V. Hessel, L. Lin, S. Meskers and F. Gallucci, *Chem. Eng. Sci.*, 2020, **220**, 115648.
55 R. Atchudan, T. N. J. I. Edison and Y. R. Lee, *J. Colloid Interface Sci.*, 2016, **482**, 8–18.
56 S. Niino, S. Takeshita, Y. Iso and T. Isobe, *J. Lumin.*, 2016, **180**, 123–131.
57 R. Atchudan, T. N. J. I. Edison, S. Perumal, R. Vinodh and Y. R. Lee, *J. Mol. Liq.*, 2019, **296**, 111817.
58 X. Li, L. Zhao, Y. Wu, A. Zhou, X. Jiang, Y. Zhan and Z. Sun, *Spectrochim. Acta, Part A*, 2022, **282**, 121638.
59 Y. Z. Guo, J. L. Liu, Y. F. Chen, Y. Q. Chai, Z. H. Li and R. Yuan, *Anal. Chem.*, 2022, **94**, 7601–7608.
60 Z. Liu, Z. Mo, N. Liu, R. Guo, X. Niu, P. Zhao and X. Yang, *J. Photochem. Photobiol., A*, 2020, **389**, 112255.
61 N. Xiao, S. G. Liu, S. Mo, N. Li, Y. J. Ju, Y. Ling, N. B. Li and H. Q. Luo, *Talanta*, 2018, **184**, 184–192.
62 Y. Liu, W. Li, P. Wu, C. Ma, X. Wu, M. Xu, S. Luo, Z. Xu and S. Liu, *Sens. Actuators, B*, 2019, **281**, 34–43.
63 S. Huang, E. Yang, J. Yao, Y. Liu and Q. Xiao, *Microchim. Acta*, 2018, **185**, 1–9.
64 H. D. Ibarra-Prieto, A. Garcia-Garcia, F. Aguilera-Granja, D. C. Navarro-Ibarra and I. Rivero-Espejel, *Nanomaterials*, 2023, **13**, 2753.

65 M. Liu, J. Liu, X. Gu, P. Kong, Y. Han, X. Wang and Z. Zheng, *J. Catal.*, 2023, **426**, 345–351.
66 J. Ding, C. Tang, G. Zhu, W. Sun, A. Du, F. He, M. Wu and H. Zhang, *ACS Appl. Energy Mater.*, 2021, **4**, 846–854.
67 M. Liu, Y. Bai, Y. He, J. Zhou, Y. Ge, J. Zhou and G. Song, *Microchim. Acta*, 2021, **188**, 1–8.
68 Z. Guo, X. Zhu, S. Wang, C. Lei, Y. Huang, Z. Nie and S. Yao, *Nanoscale*, 2018, **10**, 19579–19585.
69 Y. Yang, D. Zhang and Q. Xiang, *Nanoscale*, 2019, **11**, 18797–18805.
70 S. Chaguetmi, F. Mammeri, S. Nowak, P. Decorse, H. Lecoq, M. Gaceur, J. Ben Naceur, S. Achour, R. Chtourou and S. Ammar, *RSC Adv.*, 2013, **3**, 2572–2580.
71 W. Bao, X. Xie, J. Xu, X. Guo, J. Song, W. Wu, D. Su and G. Wang, *Chem.–Eur. J.*, 2017, **23**, 12613–12619.
72 V. Natu, M. Benchakar, C. Canaff, A. Habrioux, S. Célérier and M. W. Barsoum, *Matter*, 2021, **4**, 1224–1251.
73 Z. Guo, X. Zhu, S. Wang, C. Lei, Y. Huang, Z. Nie and S. Yao, *Nanoscale*, 2018, **10**, 19579–19585.
74 A. M. Ektessabi and S. Hakamata, *Thin Solid Films*, 2000, **377–378**, 621–625.
75 M. Schindler, F. C. Hawthorne, M. S. Freund and P. C. Burns, *Geochim. Cosmochim. Acta*, 2009, **73**, 2488–2509.
76 V. Arul and M. G. Sethuraman, *ACS Omega*, 2019, **4**, 3449–3457.
77 Z. F. Ying, D. Yu, H. Ling, N. Xu, Y. F. Lu, J. Sun and J. D. Wu, *Diam. Relat. Mater.*, 2007, **16**, 1579–1585.
78 R. Gimeno-Muñoz, R. Díaz-Torres, S. Gómez-Coca, O. Roubeau, J. M. Díaz-Cruz, N. Aliaga-Alcalde and A. González-Campo, *ACS Appl. Mater. Interfaces*, 2025, **17**, 20383–20393.
79 K. Govindaraju, T. Supreme, D. N. Labunsky, N. Martin, J. M. Del Rosario, A. Washington, E. O. Uwadiale, S. Adjei, S. Ladjadj, C. V. Melendrez, S. J. Lee, M. V. Altoe, A. Green, S. Riano, S. Sainio, D. Nordlund and A. Wolcott, *Nanomaterials*, 2024, **14**, 1274.
80 H. Sediri, D. Pierucci, M. Hajlaoui, H. Henck, G. Patriarche, Y. J. Dappe, S. Yuan, B. Toury, R. Belkhou, M. G. Silly, F. Sirotti, M. Boutchich and A. Ouerghi, *Sci. Rep.*, 2015, **5**(1), 1–10.
81 F. Yang, Y. Ge, T. Yin, J. Guo, F. Zhang, X. Tang, M. Qiu, W. Liang, N. Xu, C. Wang, Y. Song, S. Xu and S. Xiao, *ACS Appl. Nano Mater.*, 2020, **3**, 11850–11860.
82 H. Zhang, W. Qiu, Y. Zhang, Y. Han, M. Yu, Z. Wang, X. Lu and Y. Tong, *J. Mater. Chem. A*, 2016, **4**, 18639–18645.
83 R. Rajeev and A. Varghese, *J. Electrochem. Soc.*, 2024, **171**, 027504.
84 A. R. Cherian, L. Benny, A. George, U. Sirimahachai, A. Varghese and G. Hegde, *Electrochim. Acta*, 2022, **408**, 139963.
85 S. Yadav, R. Devi, P. Bhar, S. Singhla and C. S. Pundir, *Enzyme Microb. Technol.*, 2012, **50**, 247–254.
86 S. Yadav, A. Kumar and C. S. Pundir, *Anal. Biochem.*, 2011, **419**, 277–283.
87 S. Yadav, R. Devi, A. Kumar and C. S. Pundir, *Biosens. Bioelectron.*, 2011, **28**, 64–70.
88 J. Raveendran, P. E. Resmi, T. Ramachandran, B. G. Nair and T. G. Satheesh Babu, *Sens. Actuators, B*, 2017, **243**, 589–595.
89 P. Han, S. Xu, S. Feng, Y. Hao and J. Wang, *Talanta*, 2016, **151**, 114–118.